

Acceleration of relativistic protons in a CME-perturbed solar wind

A. Houeibib¹, F. Pantellini¹, and L. Griton¹

LIRA, Observatoire de Paris, Université PSL, Sorbonne Université, Université Paris Cité, CY Cergy Paris Université, CNRS, 92190 Meudon, France

.....

ABSTRACT

We investigate the impact of a Coronal Mass Ejection (CME) on the transport and acceleration of relativistic protons in the solar wind using a coupled 3D Magnetohydrodynamics (MHD) simulation and a test-particle approach. The CME is driven by a spheromak injected into a Parker solar wind at a heliocentric distance of 0.139 AU. The trajectories of 5 GeV protons, injected towards the CME from 3 AU, are integrated in the guiding-centre approximation limit and scattered in velocity space with a mean free path λ_{\parallel} . Our results show that the CME can increment the protons energy by several GeV. The acceleration occurs during the time particles stream along the portion of a magnetic field line subject to compression downstream of the quasi-perpendicular portion of the CME-driven shock. In our configuration, the maximum energy gain, which is of the order of a few percent per shock crossing, occurs when the shock approaches 0.3 AU. Large energy gains require multiple passes through the acceleration region, which is made possible by the combined action of the mirror force and pitch angle scattering. The efficiency of the acceleration on time scales of the order of hours scales as $\lambda_{\parallel}^{-3/2}$. Energy spectra harden for decreasing parallel mean free path λ_{\parallel} .

Key words. Solar energetic particles – Magnetohydrodynamics (MHD) – Sun: coronal mass ejections (CMEs) Solar wind – Acceleration of particles – Methods: numerical

1. Introduction

At Earth orbit, the interplanetary medium is mostly filled with protons and electrons at typical thermal energies of ~ 10 eV, streaming outwards from the Sun at several 10^2 km/s. In addition to these dominant components (in terms of pressure and mass density), a tenuous background of much more energetic particles is also observed. These include solar energetic particles (SEPs) accelerated during solar eruptions or at shock waves driven by coronal mass ejections (CMEs) (Desai & Giacalone 2016; Klein & Dalla 2017), reaching energies of several hundred MeV (Reames 1997). Extra-heliospheric particles, such as anomalous cosmic rays (ACRs) and galactic cosmic rays (GCRs), cover an even large range from a few MeV up to several PeV (see e.g. Lara et al. (2024) and references therein). Charged particles are sensitive to the electromagnetic field. Hence, modifications of the interplanetary electromagnetic structure by transients such as CMEs are expected to affect the transport of energetic particles throughout the heliosphere (see e.g. Cane (2000); Richardson (2004); Richardson & Cane (2011)). Many studies on the propagation of GCRs in the interplanetary medium have focused on the so-called "Forbush decrease" (Forbush 1937, 1938, 1958) : a sudden drop in the GCR intensity in the wake of a CME (Cane 2000; Dumbović et al. 2012; Kilpua et al. 2017). Less, have addressed the question of the energy gain or loss of GCRs as they interact with the CME. One reason is that embarked instruments measure flux variations of GCRs for some selected energy channels and not the changes of the kinetic energy of a single GCR. In addition spacecraft can only monitor the temporal variations at one given point in space. A more global view can be obtained by studying the propagation of GCRs in the electromagnetic field of a 3D time-dependent numerical simulations of a CME. In this work, we integrate the trajectories of individual protons in the guiding center approximation (GCA) as done

in a previous work for 86 keV electrons in a steady solar wind (see Houeibib et al. 2025). Here, the background electromagnetic field is extracted from a 3D MHD simulation of a Parker-type solar wind perturbed by one single CME. We considered the propagation of relativistic 5 GeV protons for which the GCA remains valid for the fields in a CME propagating near 1 AU. The role of pitch-angle scattering by small scale turbulence (not included in the MHD simulation) will be extensively discussed. The paper is structured as follows. The MHD simulation and the GCA equations are presented in Sect. 2. The physical mechanism responsible for the acceleration of the particles in the CME driven shock is discussed in Sec. 3. The role of scattering in Sec. 4 and a summary of the results in Sec. 5

2. Model and numerical setup

We use a MHD code to simulate a three-dimensional, time-dependent, magnetized Parker-type wind perturbed by a CME. We then propagate energetic protons in the time-dependent electromagnetic field of the MHD simulation by numerically integrating the equations of motion in the guiding-center approximation.

2.1. MHD model for the solar wind and the CME

As in Houeibib et al. (2025), we use the three-dimensional MHD code (MPI-AMRVAC) in the ideal MHD approximation to simulate the solar wind and the CME. The plasma is an ideal gas with polytropic index $5/3$. In order to convert from mass density ρ and pressure p to number density n and temperature T (which do not appear in the MHD equations) we assume a fully ionized proton-electron plasma where protons and electrons have the same tem-

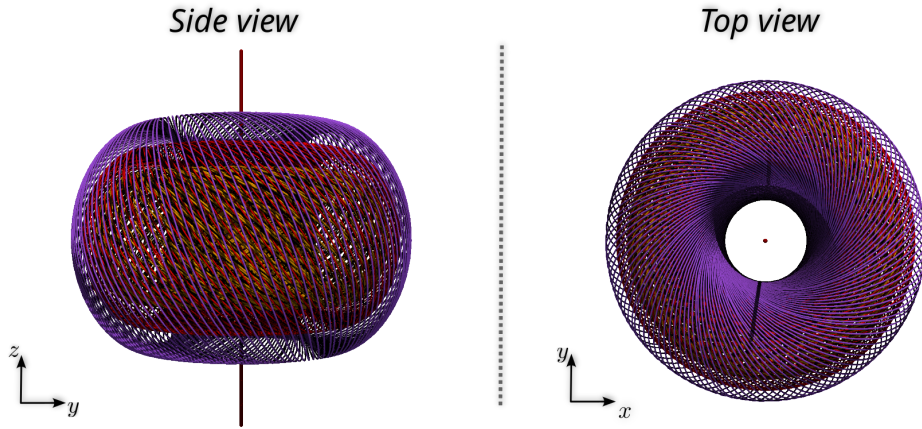


Fig. 1. Top and side views of the magnetic field lines in a spheromak. Note that despite appearances the magnetic field strength of the spheromak increases monotonically towards its center where it peaks at $2B_0/3$ (see equations (1) and (2)). At the boundary of the spheromak, at $r' = R_s$, there is only a non-zero poloidal component $B'_p = 0.2172 B_0 \sin(\theta')$.

perature $T_e = T_p = T$ and same number density $n_e = n_p = n$ implying that $\varrho = \bar{m}n$ with $\bar{m} \equiv (m_e + m_p)/2 \approx m_p/2$.

The simulation domain is a Sun-centred spherical grid of size $[144 \times 48 \times 128]$ in $[r, \theta, \varphi]$, where r is the radial coordinate, extending from $r = 0.139$ AU to $r = 13.95$ AU, θ is the polar angle, ranging from 0 to π , and φ is the azimuthal angle, ranging from 0 to 2π . The grid is uniform in θ and φ . On the other hand, to prevent an excessive longitudinal and latitudinal stretching of the cells, we adopt a stretching factor of 1.02 between adjacent cells in the direction of increasing r . For simplicity, we adopt a Parker type wind and a positive magnetic monopole located at the Sun's center, so that there is no induced heliospheric current sheet as in the case of a dipolar intrinsic field. At the Sun's surface, the monopole field strength is $2 \times 10^{-4} T$. We assume that the inner boundary is rotating rigidly with the Sun. Consequently, the tangential velocity components of the plasma at the inner boundary are prescribed as $\Omega \times r$, where $\Omega = \Omega \hat{z}$ with $\Omega = 2\pi/(30 \text{ d})$, corresponding to the angular rotation speed of the Sun. At the inner boundary, we impose a Neumann condition $\partial u_r / \partial r = 0$ to the radial component of the plasma speed u_r , a constant temperature $T = 2 \text{ MK}$ and a constant mass density $\varrho = 1.0 \times 10^{-19} \text{ kg m}^{-3}$. At the outer boundary, we impose zero-gradient conditions ($\partial/\partial r = 0$) for all physical quantities. We note that the inner boundary of the simulation domain is located beyond the sonic point, so that the wind starts supersonic at the boundary. After several rotations of the Sun the simulation reaches a steady state. Wind parameters at 1 AU in the equatorial plane of the simulation are given in Table 1. The simulated wind is somewhat underdense but otherwise typical of the real solar wind at 1 AU (Larrodera & Cid 2020; Salem et al. 2023).

Table 1. MHD simulation: wind parameters in the equatorial plane at $r = 1 \text{ AU}$. Here, p is the plasma thermal pressure, μ_0 is the permeability of vacuum.

Magnetic field strength B	4.96 nT
Wind speed u_{sw}	430 km/s
Number density n	1.10 cm^{-3}
Sound speed $c_s = (\frac{5}{3} p/\varrho)^{1/2}$	48.62 km/s
Alfvén speed $c_A = (B^2/\mu_0 \varrho)^{1/2}$	146.17 km/s
Plasma beta $\beta = p/2\mu_0 B^2$	0.13

Following previous authors (Verbeke et al. 2019; Kataoka et al. 2009; Shiota & Kataoka 2016; Singh et al. 2020; Koehn et al. 2022) a Coronal Mass Ejection (CME) is triggered by injecting a force free spheromak-type magnetic structure through the inner domain boundary. The magnetic field of a spheromak is conveniently defined using a spherical coordinates system (r', θ', ϕ') where the prime refers the spheromak frame. In this frame, for $r' \leq R_s$, the poloidal and toroidal components of the spheromak are given by:

$$\mathbf{B}'_p = B_0 \left[\left(2 \frac{j_1(\lambda r')}{\lambda r'} \cos \theta' \right) \mathbf{e}'_r - \left(j_0(\lambda r') - \frac{j_1(\lambda r')}{\lambda r'} \right) \sin \theta' \mathbf{e}'_{\theta'} \right], \quad (1)$$

$$\mathbf{B}'_t = H B_0 j_1(\lambda r') \sin \theta' \mathbf{e}'_{\phi'}. \quad (2)$$

For $r' > R_s$ all components are set to zero. In equations (1) and (2), B_0 is a reference field strength, $j_{0,1}$ the first two spherical Bessel functions and $\lambda \approx 4.493409/R_s$ such that $j_1 = 0$ at the edge of the spheromak at $r' = R_s$. We note that at $r' = R_s$, the toroidal field B'_t vanishes while the poloidal field reduces to $B'_p = 0.21723 B_0 \sin \theta' \mathbf{e}'_{\theta'}$. $H = \pm 1$ defines the handedness of the magnetic structure via the orientation of the toroidal field. In our simulation we set $B_0 = 144 \text{ nT}$ and $R_s = 10.5 R_{\odot}$.

As shown in Figure 2, the spheromak is introduced into the simulation through its inner domain boundary in the equatorial plane (defined by the Sun's rotation) at a constant radial speed of $V_s = 1028 \text{ km/s}$. The axis of the spheromak has been oriented perpendicularly to the equatorial plane. The mean values of the plasma density and temperature in the spheromak are $n = 65 \text{ cm}^{-3}$ and $T = 0.6 \text{ MK}$, respectively.

The equatorial cuts in Fig. 3 shows temporal snapshots of the fluid temperature and radial velocity which both trace the propagation of the shock front through its heating and acceleration of the fluid it encounters. The inner edge of the high temperature arc also delimits the discontinuity separating the fluid heated by the shock from the magnetic driver of the CME (the spheromak "remnant").

In Figure 4 we report the temporal profiles for various plasma parameter measured at a fixed position at 1 AU , represented by the cross in Figure 3. The time sequence can be decomposed as follows:

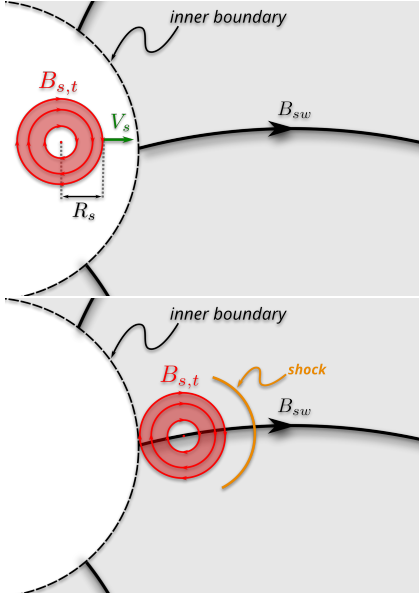


Fig. 2. Injection of the spheromak into the numerical domain. Top panel : the spheromak is injected in the equatorial plane at a constant radial speed V_s in a pre-existing stationary wind.

- **Shock arrival:** The shocks reaches the observation point at $t \approx 28$ hours after the spheromak's injection when the density rises by a factor 3 and the magnetic field intensity from ~ 5 nT to ~ 11 nT.
- **Sheath region :** Between $t \approx 28$ h and $t \approx 50$ h, the observation point is in region of plasma compressed and heated by the shock.
- **CME Core (Ejecta) :** Between $t \approx 50$ h and $t \approx 130$ h, the observation point is in the ejecta (the spheromak "remnant"). During the early phase of the period, the magnetic field lines move eastward ($u_{E,y} > 0$) instead of general westward motion in the unperturbed wind (also see Figure 5). For $t \gtrsim 130$ h, the profiles slowly recover pre-shock conditions.

2.2. The guiding center equations

Hereafter, we consider the motion of 5 GeV protons injected on three selected equatorial field lines in the CME perturbed solar wind described in Section 2. The three field lines, numbered 0, 1, and 2 evolve in time as shown in Figure 5. Hence, unlike Houeibib et al. (2025) who considered steady fields, we use the GC equations for the case of time-varying \mathbf{E} and \mathbf{B} fields. In the limit $|v_E| = |\mathbf{E} \times \mathbf{b}/B| \ll c$ (c is speed of light), they can be written in the following form:

$$\frac{d\mathbf{R}}{dt} = v_{\parallel}\mathbf{b} + \mathbf{v}_E + \frac{\gamma m}{qB}\mathbf{b} \times \left[\frac{v_{\parallel}}{\gamma} \frac{qE_{\parallel}}{mc^2} \mathbf{v}_E + \frac{\mu_B}{\gamma^2 m} \left(\nabla B + \frac{\mathbf{v}_E}{c^2} \partial_t B \right) + v_{\parallel} D_t \mathbf{b} + D_t \mathbf{v}_E \right] \quad (3)$$

$$\frac{d(\gamma v_{\parallel})}{dt} = \frac{q}{m} E_{\parallel} - \frac{\mu_B}{\gamma m} \mathbf{b} \cdot \nabla B + \gamma \mathbf{v}_E \cdot D_t \mathbf{b} \quad (4)$$

$$\frac{d\mu_B}{dt} = 0. \quad (5)$$

with $D_t(*) = \partial_t(*) + (v_{\parallel}\mathbf{b} + \mathbf{v}_E) \cdot \nabla(*)$. Note the factor q/mc^2 in (3) which was mistakenly omitted in equation (1) of Houeibib

et al. (2025). In the above equations, the subscripts \parallel and \perp indicate projections parallel and perpendicular to \mathbf{B} . \mathbf{R} is the particle's guiding centre position, \mathbf{v} its velocity, $\gamma \equiv 1/\sqrt{1-v^2/c^2}$ its Lorentz factor, $\mu_B \equiv \frac{1}{2}m\gamma^2 v_{\perp}^2/B$ its magnetic moment, $\mathbf{b} \equiv \mathbf{B}/B$, and $\mathbf{v}_E \equiv \mathbf{E} \times \mathbf{b}/B$. Numerically, particles are advanced in time using the third-order accurate predictor-corrector scheme used by Houeibib et al. (2025) (also see Mignone et al. (2023)) with all fields and derivatives of the fields on the right-hand-side of the above GC equations computed within the MHD code and linearly interpolated from the MHD grid to the particle's position. The integration time step Δt is given by : $\Delta t = \min(L_B, \lambda_{\parallel})/c$, where c is the speed of light, $L_B \equiv (|\nabla_{\parallel} B|/B)^{-1}$ and λ_{\parallel} the scattering mean-free path (see Section 4). Although the structure of the GCA equations is much more complex than that of the full equations of motion, they offer a considerable advantage by eliminating the need for an integration time step smaller than the particle gyration period. This approach enables the integration of particle trajectories with higher precision and longer time scales at reduced computational costs.

3. Time evolution of a proton in the field of the CME (no scattering)

Let us first consider the propagation of a single 5GeV proton injected on the magnetic field line 0, some ~ 1.5 days after the spheromak injection (red line in bottom-left panel of Fig. 5). The particle is initially positioned at $r = 3$ AU with a pitch-angle $\alpha = 170^\circ$ (travelling towards the Sun) in order to be mirror reflected before reaching the inner boundary. The speed of a relativistic proton largely exceeds that of the CME so that during its round trip one may the fields to be static, i.e. $\partial/\partial t = 0$ in (4). Also considering that $E_{\parallel} \ll E_{\perp}$ (generally verified in the solar wind), we conclude that the proton's kinetic energy $\mathcal{E} = (\gamma - 1)mc^2$ evolves according to

$$\begin{aligned} \frac{d\mathcal{E}}{dt} &\simeq m\gamma v_{\parallel}^2 \mathbf{v}_E \cdot (\mathbf{b} \cdot \nabla) \mathbf{b} + m\gamma \frac{v_{\perp}^2}{2} \mathbf{v}_E \cdot \nabla \ln B \\ &\simeq m\gamma v_{\parallel}^2 \mathbf{v}_E \cdot (\mathbf{b} \cdot \nabla) \mathbf{b} + \frac{\mu_B}{\gamma} \mathbf{v}_E \cdot \nabla B. \end{aligned} \quad (6)$$

In the above equation, the right hand side terms correspond to the energy gain due to the curvature and gradient drifts, respectively. Noting that the energy variation $d\mathcal{E}/dt$ associated to each term can be written as $qv_d \cdot \mathbf{E}$, where v_d is the corresponding drift velocity, we plot their relative contributions in Fig. 6. The acceleration is clearly ascribable to the gradient drift term. We denote $\Delta t_c \approx 0.05$ h as the time interval of strong acceleration, occurring in two stages, at $t \approx 0.6$ h and $t \approx 0.9$ h (see Figure 6). Both phases of acceleration occur during the period of time when the particle is located downstream of the shock where $\mathbf{v}_E \cdot \nabla B > 0$. The first acceleration step takes place as the particles moves inwards (towards the Sun), the second as the particle moves outwards after reflection at its mirror point. The energy gain can therefore be written as

$$\Delta \mathcal{E} \simeq \frac{\mu_B}{\gamma} \Delta t_c \mathbf{v}_E \cdot \nabla B \quad (7)$$

or, in terms of relative variation, as

$$\frac{\Delta \mathcal{E}}{\mathcal{E}} \simeq \frac{1}{2} \frac{\gamma^2}{\gamma(\gamma-1)} \frac{v_{\perp}^2}{c^2} \Delta t_c \mathbf{v}_E \cdot \frac{\nabla B}{B} \propto \Delta t_c \mathbf{v}_E \cdot \frac{\nabla B}{B}. \quad (8)$$

Equations (7) and (8) show that the gain of energy is due the advection, towards regions of increasing B field intensity, of the

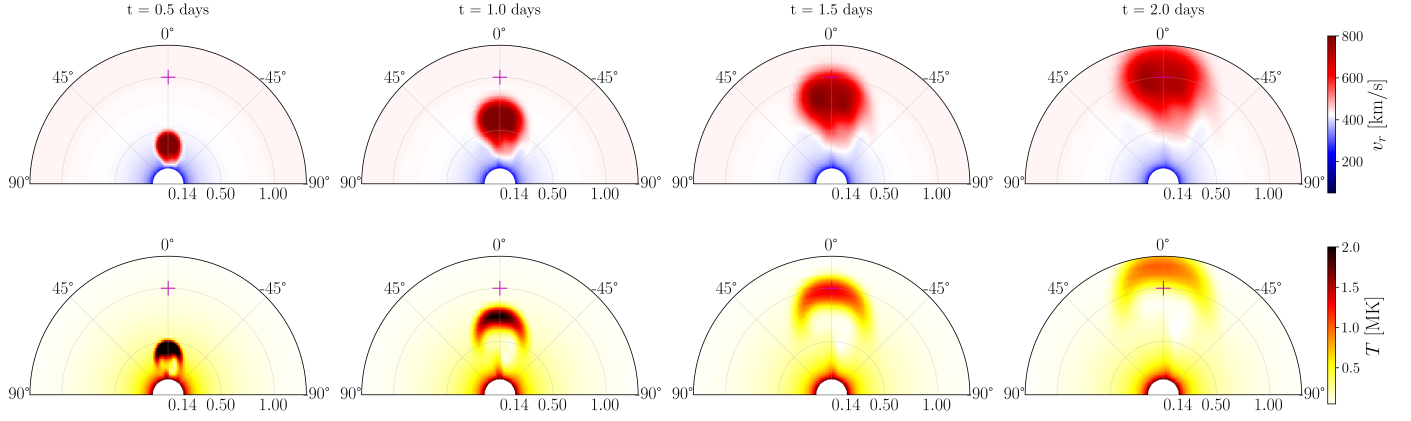


Fig. 3. Equatorial cuts of the simulation domain as a function of time, where the time $t=0$ corresponds to the injection time of the spheromak. The color maps are for the radial fluid velocity (top panel) and temperature (bottom panel).

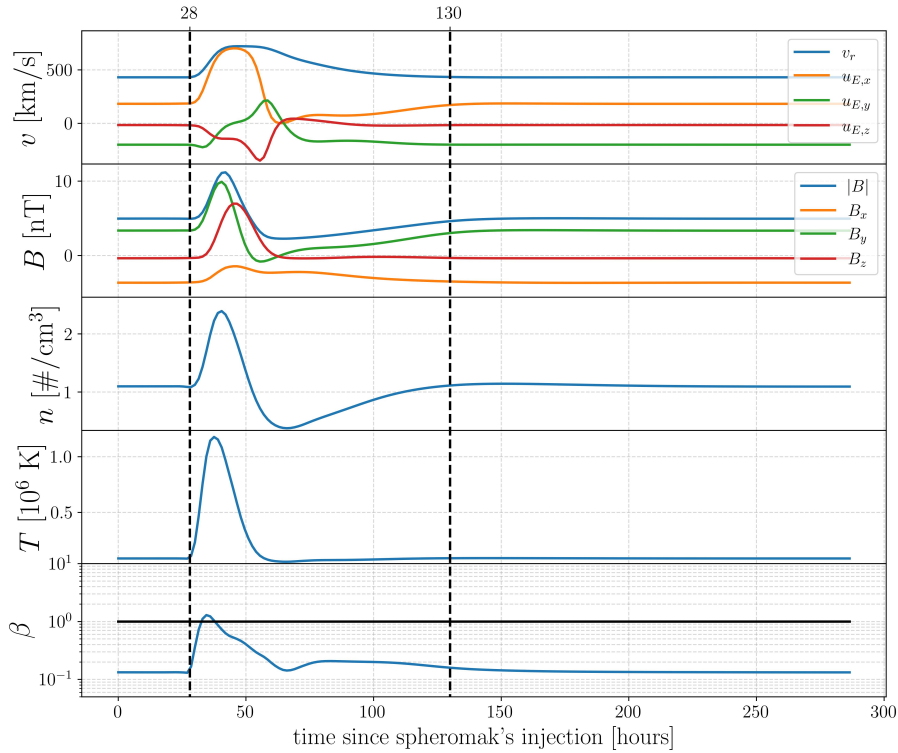


Fig. 4. CME induced variations of the plasma parameters at 1 AU. The vertical lines approximately delimit the time interval during which the local plasma can be considered to be perturbed by the CME.

magnetic field along which the particle is moving. The gain of energy is proportional to Δt_c , i.e. proportional to the time the particle spends in the region where $\mathbf{v}_E \cdot \nabla \mathbf{B} > 0$.

In Fig. 8 we trace the energy gain of a fictitious 5 GeV proton (and same μ_B as in Fig. 6) moving along field line 0, at different phases of the CME's expansion. Clearly, efficiency peaks when the time the CME reaches $r \approx 0.3$ AU, when the product of the three terms $\Delta t_c \mathbf{v}_E \cdot \nabla \mathbf{B}$ in equation (7) is at its maximum. The

red diamond is the gain expected for a particle encountering the CME at 1AU, which is the for the particle in Fig. 6.

4. Protons in the field of a CME (with scattering)

In Section 3, we did not consider the effect scattering in velocity space due to the particle's interaction with small scale plasma turbulence not retained in the large scale MHD simulation. In the absence of scattering, the injected particles cross the CME at

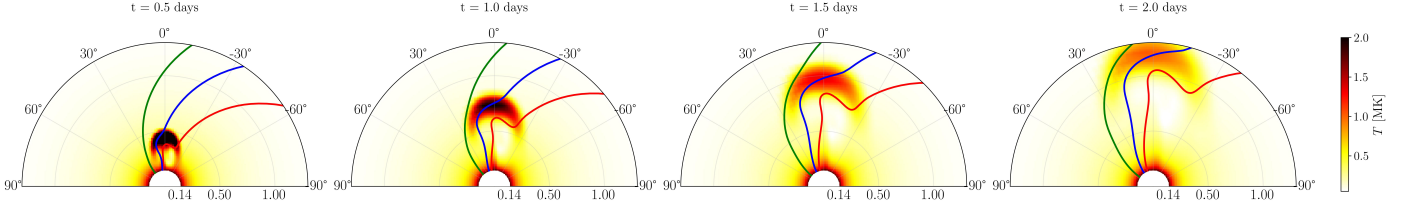


Fig. 5. Time evolution of three selected magnetic field lines, denoted 0,1 and 2 from east to west.

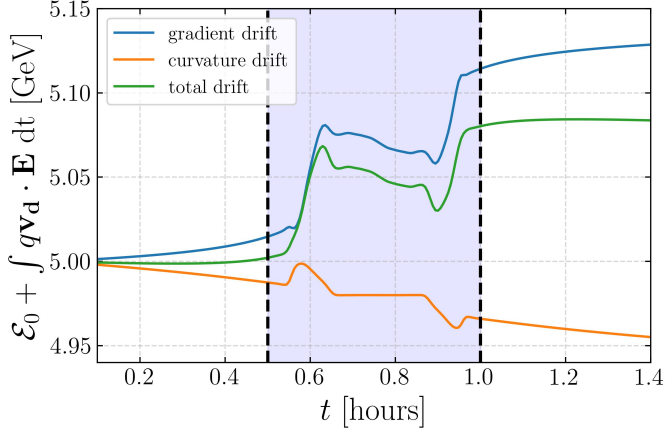


Fig. 6. Contributions to the energy variations of a 5 GeV proton moving throughout the CME perturbed plasma along line 0. In this figure, $t = 0$, corresponds to the time of injection of the particle into the system. The first increment at $t \approx 0.6$ h occurs as the particle moves towards the Sun, the second at $t \approx 0.9$ h as the particle moves away from the Sun after reflection at its mirror point. The dotted vertical lines delimit the period when the particle is inside the CME perturbed region (see the gray curve in Fig. 7)

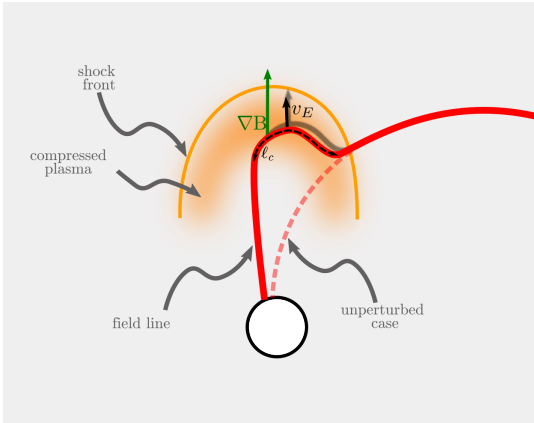


Fig. 7. Sketch representing the configuration of the perturbed field line. The gray section of length $\ell_c = c\Delta t_c$ is the portion of trajectory where $\mathbf{v}_E \cdot \nabla B > 0$ and particles can gain energy according to equation (7).

most two times; the first time as they stream towards the Sun and a second time as they stream away from the Sun after reflection at their mirror point. In the presence of scattering multiple crossings become possible. In this section, we let particles be pitch-angle scattered with a parallel mean free path λ_{\parallel} . Two different values 0.1 AU and 0.5 AU are considered, covering the gener-

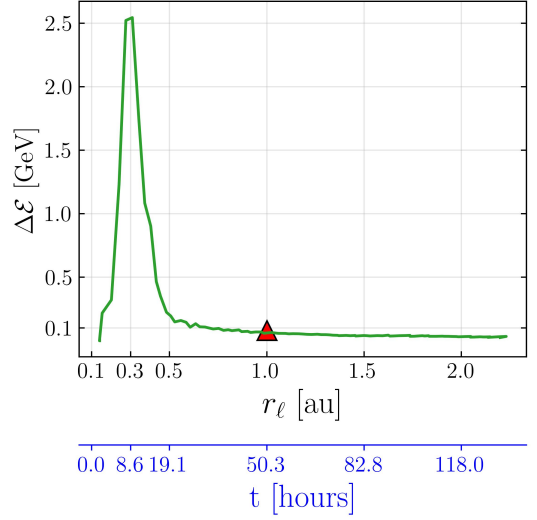


Fig. 8. Energy gain estimated from equation (7) for a fictitious proton moving along the portion of the line 0 located downstream of the quasi-perpendicular shock of the CME at different phases of its expansion. The same 5 GeV proton as the one in Fig. 6 has been assumed. Time $t = 0$ corresponds to the injection of the CME through the inner boundary of the simulation.

ally accepted range for a wide range of energies at 1 AU (Palmer 1982; Bieber et al. 1994). Particles are hard-sphere scattered by scattering centers at rest in the solar wind frame (see section 2.3 in Houeibib et al. (2025) for details).

To make statistics, we consider 10^4 mono-energetic protons of 5 GeV impulsively injected towards the Sun at $t = 0$ h with a pitch angle $\alpha = 180^\circ$. As in (Houeibib et al. 2025), particles reaching the boundaries at $r=0.14$ AU and $r=3$ AU are instantly re-injected at $r=3$ AU on the same field line and with the same initial conditions implying a constant number of particles in the domain. A particle subject to scattering may repeatedly cross the CME as it bounces back and forth between scattering centers or between mirror points and scattering centers. Given that on some privileged magnetic field lines, particles gain energy at each crossing, much larger energies can be achieved than in the no-scattering case of Section 3 provided the accelerating due to $\mathbf{v}_E \cdot \nabla B > 0$ is sufficiently strong and long lasting. In order to illustrate the role of scattering, the 4 days cumulative energy distribution for protons injected along the field lines 0, 1, and 2 are shown in figure 9 for the case $\lambda_{\parallel} = 0.5$ AU. The distributions are obtained by measuring the particles' energies as they cross the spherical shell of radius 1 AU. The figure shows that acceleration is highest on line 0 and lowest on line 2. This is not very surprising as the three field lines are very unequally affected by the

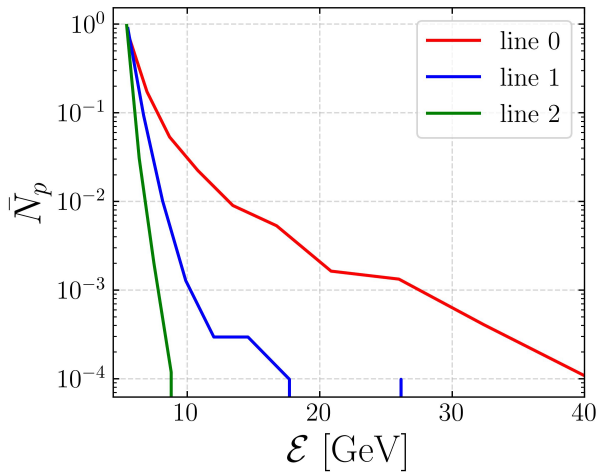


Fig. 9. Cumulative energy spectra measured at 1 AU during a time interval of ~ 4 days for 5 GeV protons injected on the three different field lines subject to scattering with a mean free path $\lambda_{\parallel} = 0.5$.

CME, with line 0 being the one with the longest portion in the region of strong magnetic compression (see Figure 5). We anticipate, that for reasonable values of λ_{\parallel} , the spectra harden with decreasing λ_{\parallel} . Indeed, by reducing λ_{\parallel} , the particles' residence time in the acceleration region increases (also see ?). The effect is illustrated in Fig. 10 where the cumulative spectra on line 0 are shown for the case $\lambda_{\parallel} = 0.5$ AU and 0.1 AU, respectively. A semi-quantitative explanation can be given by observing that in a one-dimensional diffusion experiment where N particles moving at a speed c are instantly injected at $x = 0$, the number density at any given point in space decreases asymptotically with time t as $(\pi\lambda_{\parallel}ct)^{-1/2}$. As the number of collisions experienced by a particle grows as $N_c = ct/\lambda_{\parallel}$ and since the gain of energy $\Delta\mathcal{E}$ for a particle is approximately proportional to the number of collisions $\Delta\mathcal{E} = N_c\delta\mathcal{E}$ ($\delta\mathcal{E}$ is the energy gain per passage in the acceleration region), one obtains that the number of particles gaining an energy $\delta\mathcal{E}$ scales as $(ct/\lambda_{\parallel}^3)^{1/2} \propto \lambda_{\parallel}^{-3/2}$. Consequently, reducing the mean free path, increases the number of particles gaining a given energy $\Delta\mathcal{E}$. In our case, the number of particles accelerated to a given energy is expected to be larger by a factor $(0.5/0.1)^{3/2} \approx 11.2$ for the case $\lambda_{\parallel} = 0.1$ AU with respect to the case $\lambda_{\parallel} = 0.5$ AU. This is effectively the factor separating the two curves in Fig. 10.

5. Conclusions

We compute the guiding center trajectories of relativistic 5 GeV protons in the field of a MHD simulation of a Parker-type solar wind perturbed by an equatorial CME. The CME is triggered by the gradual insertion of a spheromak through the inner boundary of the simulation domain at $r = 0.139$ AU. The protons are injected sunwards, from a heliocentric distance of 3 AU, along three equatorial magnetic field lines crossing the CME at different heliographic longitudes. The main findings are summarized below.

1. Particles gain energy as they travel through the compressed plasma downstream of the CME-driven shock. The acceleration occurs in places where the magnetic field line guiding the particle is advected towards regions of growing field strength by the $v_E = \mathbf{E} \times \mathbf{B}/B^2$ drift.

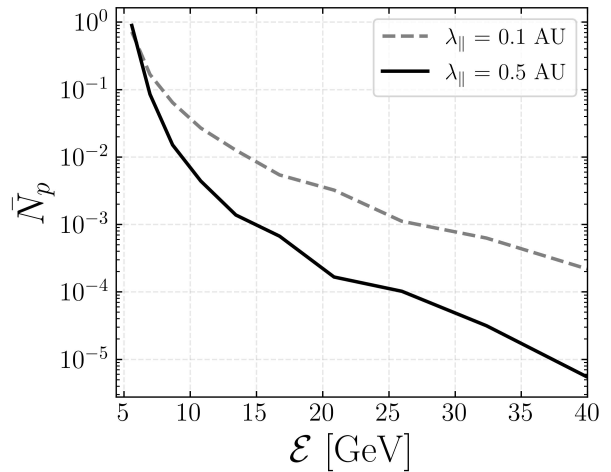


Fig. 10. Cumulative energy spectra of particles at 1 AU on line 0, for two different values of λ_{\parallel} during a time interval of ~ 4 days. The difference between the two curves is compatible with a $\lambda_{\parallel}^{-3/2}$ scaling factor.

2. A peak energy gain of up to $\sim 50\%$ for one single CME crossing has been observed at the time the CME shock front reaches 0.3 AU.
3. In the case of pitch angle scattering, particles may cross the CME multiple times and reach substantially higher energies. For example, assuming hard sphere type scattering and a mean free path $\lambda_{\parallel} = 0.1$ AU, some 0.1% of the injected particles increase their energy by a factor six in 4 days.
4. The efficiency of the acceleration strongly depends on where the particle encounters the shock. For the three equatorial field lines considered, efficiency increases westward (see Figures 5 and 9).
5. The energy distributions harden for decreasing λ_{\parallel} as the number of times the particles flow through the region of acceleration increases. The number of particles reaching a given energy is effectively found to scale as $\lambda_{\parallel}^{-3/2}$.

Acknowledgements. This work has been financially supported by the PLAS@PAR project and by the National Institute of Sciences of the Universe (INSU). AH is supported by the CNES (Centre National d'Études Spatiales).

References

- Bieber, J. W., Matthaeus, W. H., Smith, C. W., et al. 1994, *ApJ*, 420, 294
Cane, H. V. 2000, *Space Sci. Rev.*, 93, 55
Desai, M. & Giacalone, J. 2016, *Living Reviews in Solar Physics*, 13, 3
Dumbović, M., Vršnak, B., Čalogović, J., & Župan, R. 2012, *A&A*, 538, A28
Forbush, S. E. 1937, *Physical Review*, 51, 1108
Forbush, S. E. 1938, *Physical Review*, 54, 975
Forbush, S. E. 1958, *J. Geophys. Res.*, 63, 651
Houeibib, A., Pantellini, F., & Griton, L. 2025, *A&A*, 694, A211
Kataoka, R., Ebisuzaki, T., Kusano, K., et al. 2009, *Journal of Geophysical Research (Space Physics)*, 114, A10102
Kilpua, E., Koskinen, H. E. J., & Pulkkinen, T. I. 2017, *Living Reviews in Solar Physics*, 14, 5
Klein, K.-L. & Dalla, S. 2017, *Space Sci. Rev.*, 212, 1107
Koehn, G., Desai, R. T., Davies, E. E., et al. 2022, *ApJ*, 941, 139
Lara, A., Borgazzi, A., Guennam, E., Niembro, T., & Arunbabu, K. P. 2024, *Journal of Geophysical Research: Space Physics*, 129, e2024JA032478
Larrodera, C. & Cid, C. 2020, *A&A*, 635, A44
Mignone, A., Haudemand, H., & Puzzone, E. 2023, *Computer Physics Communications*, 285, 108625
Palmer, I. D. 1982, *Reviews of Geophysics*, 20, 335
Reames, D. V. 1997, *Geophysical Monograph Series*, 99, 217
Richardson, I. G. 2004, *Space Sci. Rev.*, 111, 267
Richardson, I. G. & Cane, H. V. 2011, *Sol. Phys.*, 270, 609

- Salem, C. S., Pulupa, M., Bale, S. D., & Verscharen, D. 2023, *A&A*, 675, A162
Shiota, D. & Kataoka, R. 2016, *Space Weather*, 14, 56
Singh, T., Yalim, M. S., Pogorelov, N. V., & Gopalswamy, N. 2020, *ApJ*, 894,
49
Verbeke, C., Pomoell, J., & Poedts, S. 2019, *A&A*, 627, A111